

See discussions, stats, and author profiles for this publication at: <https://www.researchgate.net/publication/262934156>

Quantitative Spectral Analysis of Coherent Anti-Stokes Raman Scattering Signals: C-H Stretching Modes of the Methyl Group

ARTICLE in THE JOURNAL OF PHYSICAL CHEMISTRY B · JUNE 2014

Impact Factor: 3.3 · DOI: 10.1021/jp5035807

CITATIONS

2

READS

35

4 AUTHORS, INCLUDING:



Chi Zhang

Purdue University

33 PUBLICATIONS 222 CITATIONS

SEE PROFILE



Bei Ding

University of Pennsylvania

11 PUBLICATIONS 153 CITATIONS

SEE PROFILE



Joshua Jasensky

University of Michigan

24 PUBLICATIONS 139 CITATIONS

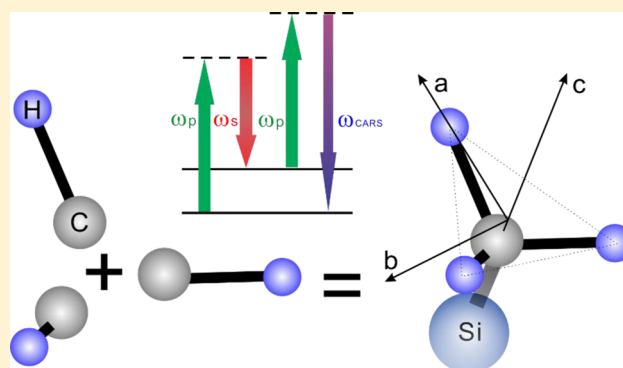
SEE PROFILE

Quantitative Spectral Analysis of Coherent Anti-Stokes Raman Scattering Signals: C–H Stretching Modes of the Methyl Group

Chi Zhang,^{*,†} Jie Wang,^{†,§} Bei Ding,[†] and Joshua Jasensky[‡][†]Department of Chemistry and [‡]Department of Biophysics, University of Michigan, 930 North University Avenue, Ann Arbor, Michigan 48109, United States

S Supporting Information

ABSTRACT: Coherent anti-Stokes Raman scattering (CARS) vibrational spectroscopy has been extensively developed into a powerful analytical technique to study various molecules. Quantitative interpretation of CARS spectra can help to improve CARS for chemical analysis and extend its analytical applications. In this work, we quantitatively analyzed CARS signals originating from the methyl groups in poly-(dimethylsiloxane) (PDMS), with the help of the bond additivity method. Experimentally, a home-built CARS spectrometer modified from a commercial sum frequency generation spectrometer was used to collect CARS spectra from a PDMS film. Theoretically, we successfully reproduced the peak intensity ratio of C–H symmetric and asymmetric stretching modes of the PDMS methyl group in different polarization combinations based on bond additivity method and Raman depolarization ratio. This research shows that bond additivity theory can help to obtain the third-order nonlinear susceptibility tensor properties probed by different polarization combinations used in CARS spectroscopy. The method developed in this work could also be applied to CARS vibrational stretching analysis of other functional groups, providing quantitative understanding of CARS spectrum for applications in spectroscopy.



1. INTRODUCTION

Since the first report of the coherent anti-Stokes Raman scattering (CARS) phenomenon,¹ CARS as a Raman spectroscopy technique has gradually developed into a powerful analytical tool for chemical, material, and biological analysis. CARS is a coherent four-wave mixing process resulting in a coherent anti-Stokes Raman signal which is many orders of magnitude stronger than the spontaneous Raman signal. The anti-Stokes Raman signal is generated at a wavelength shorter than the input laser beams and, thus, can effectively eliminate possible one-photon fluorescence background in spectral data. The stronger and directional signal also leads to a significant reduction in signal collection time as compared to spontaneous Raman measurement. The above advantages grant CARS unique applications in many areas. The theory and applications of CARS have seen years of successful and systematic development,² with many studies focusing on the behavior of gases,^{3–10} liquids or solutions,^{11–14} and solid phase materials.^{15–19} It has also been developed as a tool for the standoff detection of explosive materials.^{20–25}

Additionally, CARS microscopy has been developed for biological and material studies.^{25–29} With the help of laser scanning, image collection as fast as video-rate has been achieved.³⁰ Thanks to rapid advancement of laser technologies and the excellent research efforts from various research groups, CARS microscopy systems have been significantly improved

with better sensitivity, lower nonresonant background, broader spectral imaging windows, stronger capability, and wider applications.^{31–38} CARS microscopy has been extensively applied to lipid detection and diagnosis.^{39–43} Various technical improvements have been made on CARS microscopy such as epidection CARS,⁴⁴ polarization sensitive CARS,³⁴ heterodyne CARS,³⁷ interferometry CARS,⁴⁵ single pulse CARS,⁴⁶ holographic CARS,⁴⁷ hyperspectral CARS,^{48,49} and so forth. Quantitative spectral analysis methods have also been developed to improve CARS interpretation.^{50–52} Such works have advanced CARS to become a powerful microscopy and imaging tool for biomedical applications.

Although significant advancement of technical development and applications in CARS have been made in the last two decades, theoretical work, especially quantitative physical interpretation of CARS spectrum based on molecular symmetries, has had fewer contributions. Such quantitative understanding of the basic third-order nonlinear susceptibility under different symmetry conditions is important for advanced CARS spectral analysis and imaging applications. One of the key aspects of such quantitative interpretation lies on the explanation and prediction of ratios between different susceptibility tensor

Received: April 11, 2014

Revised: June 6, 2014

Published: June 9, 2014

elements of functional group vibrational modes in a molecule. Obtaining such information requires a theoretical connection between the macroscopic nonlinear susceptibility tensor and the hyperpolarizabilities of the molecular vibrations considering their properties under different molecular symmetry conditions. Such an understanding can help predict CARS vibrational intensity relationships of different vibrational modes of a certain functional group, which can also help to improve vibrational peak assignments in CARS spectra. For third-order nonlinear optical processes, the vibrational transition selection rules have previously been studied systemically considering different molecular symmetry arrangements.⁵³ However, a detailed quantitative understanding on the relationship in signal intensity between different vibrational modes of a functional group has not been explored. For second-order nonlinear vibrational spectroscopies such as sum frequency generation (SFG) spectroscopy, such theoretical understanding has been systemically developed.^{54–59} One of the most widely used methods in such study, bond additivity method, has been applied to quantitatively interpret SFG spectra.^{55,60–63} Using the bond additivity model, the ratios of second-order hyperpolarizability tensor elements of a functional group with C_{3v} , C_{2v} , or other symmetry arrangements were obtained for their different vibrational modes and have shown good agreement with the experimental results.

In this work, we demonstrate the use of bond additivity method to quantitatively interpret relative intensities of CARS signals from different vibrational modes of a molecule considering the molecular symmetries. Theoretical connections between CARS and Raman measurements were established with the help of bond additivity method and Raman depolarization ratio. CARS vibrational intensities from different vibrational modes of PDMS methyl groups under different polarization combination measurements were deduced theoretically. The deduced results well matched experimental data obtained using a home-built CARS spectrometer. The theoretical approach presented in this work can be applied to quantitatively analyze CARS signals generated by vibrational modes from other functional groups or molecules.

2. THEORY

2.1. CARS Spectroscopy. CARS is a third-order nonlinear optical process. Its signal intensity is related to the input laser beam intensities through the following equation

$$I_{\text{CARS}} \propto |\chi_{\text{eff}}^{(3)}|^2 I_p^2 I_s \quad (1)$$

Here, I_{CARS} is the output CARS signal intensity, I_p is the intensity of the input pump or probe beam and I_s is the intensity of the input Stokes beam. In most CARS experiments, pump and probe share the same laser beam. $\chi_{\text{eff}}^{(3)}$ is the effective third-order nonlinear optical susceptibility of the sample generating CARS signal, which can be expressed as

$$\chi_{\text{eff}}^{(3)} = \chi_{\text{NR}}^{(3)} + \frac{\mathbf{A}_T}{\omega_T - 2\omega_p - i\Gamma_T} + \frac{\mathbf{A}_R}{\omega - (\omega_p - \omega_s) - i\Gamma_R} \quad (2)$$

The first term $\chi_{\text{NR}}^{(3)}$ is the nonresonant contribution from virtual states; the second term is the enhanced nonresonant contribution from the two-photon electronic resonance; the third term is the vibrational resonance contribution from the coherent Raman transition.²⁶ ω_T is the electronic transition frequency, typically reached by two-photon absorption; ω_p is

the pump/probe beam frequency; ω_s is the Stokes beam frequency; ω is the output or signal frequency. \mathbf{A}_T and \mathbf{A}_R are amplitudes of the two-photon absorption transition and the Raman transition, respectively; Γ_T and Γ_R are damping factors of the two-photon and Raman transitions, respectively. Contributions of the first two terms, especially the second one, is usually responsible for the strong nonresonant line-shape distortion in CARS spectroscopy. In this research, we focus on the study of the third term, due to its relation to the vibrational transition that carries the fingerprint chemical information on the sample and also dominates our spectrum. Theoretically, CARS spectra can be fit using eq 2. For samples with negligible two-photon absorption, the second term can be combined with the first term, and the contributions of the first two terms can be treated as a constant.

The CARS experimental geometry used in this study is shown in Figure 1a. The energy diagram of the CARS process is

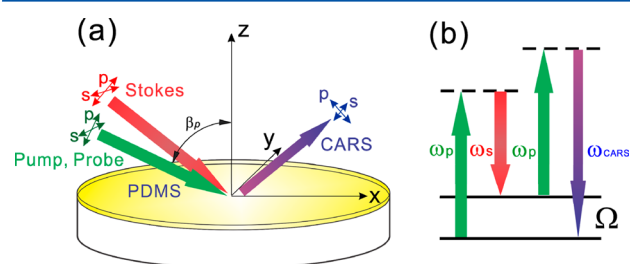


Figure 1. (a) CARS experimental geometry used in this study. The pump/probe and Stokes beams lie in the x – z plane. The s and p polarizations are defined as perpendicular and parallel with respect to the x – z plane, respectively. (b) Energy diagram of the CARS process.

shown in Figure 1b. We collected CARS signal of poly-(dimethylsiloxane) (PDMS) deposited on an optical window (fused silica window) in a “reflective” geometry. We only consider thick sample condition (sample thickness \gg the CARS signal coherent length). Under this condition, the signal is insensitive to the sample thickness and eq 1 can be generally applied without considering the sample thickness effect. Here, polarized CARS measurement was performed. For a specific vibrational mode, the effective third-order nonlinear susceptibility elements $\chi_{\text{eff},ABCD}^{(3)}$ can be correlated to the local nonlinear susceptibility elements $\chi_{IJKL}^{(3)}$ (defined in the lab frame coordinate system (x, y, z)) of the sample through the following equation

$$\chi_{\text{eff},ABCD}^{(3)} = \sum_{IJKL=x,y,z} M \cdot L_{AI}(\omega_{\text{CARS}}) L_{BJ}(\omega_p) L_{CK}(\omega_p) L_{DL}(\omega_s) \cdot \chi_{IJKL}^{(3)} \quad (3)$$

$A, B, C, D = s, p$

Here, L_{AI} , L_{BJ} , L_{CK} , L_{DL} are local field correction coefficients of the input and output laser beams, known as the Fresnel coefficients.⁵⁸ The equations to calculate such Fresnel coefficients and their deduced values in this work are listed in the Supporting Information. M is a factor that combines (multiplies) all the trigonometric factors of the input electric field projected on the lab frame coordinate axis as demonstrated in Figure 1a.⁶⁴ A, B, C, D indices represent polarization combinations (s or p) of the CARS experiment; I, J, K, L indices represent coordinates in the lab frame system (x, y, z) as shown in Figure 1a. The polarization combination “ABCD” indicates the following: A polarized CARS signal beam; B polarized

pump beam; C polarized probe beam; D polarized Stokes beam. Giving two specific examples of eq 3

$$\chi_{\text{eff},\text{ssss}}^{(3)} = 1 \cdot L_{\text{sy}}(\omega_{\text{CARS}}) L_{\text{sy}}(\omega_p) L_{\text{sy}}(\omega_p) L_{\text{sy}}(\omega_s) \cdot \chi_{\text{yyyy}}^{(3)} \quad (4)$$

$$\begin{aligned} \chi_{\text{eff},\text{spps}}^{(3)} = & \cos^2 \beta_p \cdot L_{\text{sy}}(\omega_{\text{CARS}}) L_{\text{px}}(\omega_p) L_{\text{px}}(\omega_p) L_{\text{sy}}(\omega_s) \cdot \chi_{\text{yxxxy}}^{(3)} \\ & + \cos \beta_p \sin \beta_p \cdot L_{\text{sy}}(\omega_{\text{CARS}}) L_{\text{px}}(\omega_p) L_{\text{pz}}(\omega_p) L_{\text{sy}}(\omega_s) \cdot \chi_{\text{yxzy}}^{(3)} \\ & + \sin \beta_p \cos \beta_p \cdot L_{\text{sy}}(\omega_{\text{CARS}}) L_{\text{pz}}(\omega_p) L_{\text{px}}(\omega_p) L_{\text{sy}}(\omega_s) \cdot \chi_{\text{yzxy}}^{(3)} \\ & + \sin^2 \beta_p \cdot L_{\text{sy}}(\omega_{\text{CARS}}) L_{\text{pz}}(\omega_p) L_{\text{pz}}(\omega_p) L_{\text{sy}}(\omega_s) \cdot \chi_{\text{yzzzy}}^{(3)} \end{aligned} \quad (5)$$

$\chi_{\text{eff},\text{ssss}}^{(3)}$ only has one nonzero corresponding local susceptibility term $\chi_{\text{yyyy}}^{(3)}$ because the s-polarized electric field is along the y axis. $\chi_{\text{eff},\text{spps}}^{(3)}$ has four terms because the p-polarized electric field can be projected on both the x and z axes. β is the incidence angle of the laser beam (β_p is the incidence angle of the pump/probe beam). The projection onto the x axis generates $\cos \beta_p$ and the projection onto z axis leads to $\sin \beta_p$. These examples show that the measured effective third-order nonlinear susceptibility components under certain polarization combinations can be related to the local third-order nonlinear susceptibility components of the sample.

The next step is to correlate the local third-order nonlinear susceptibility to the molecular hyperpolarizability $\chi_{ijkl}^{(3)}$. Such a relation can be expressed as

$$\chi_{IJKL}^{(3)} = N \sum_{ijkl=x,y,z} \langle R_{Li} R_{Jj} R_{Kk} R_{Ll} \rangle \chi_{ijkl}^{(3)} \quad ijkl = a, b, c \quad (6)$$

$$\begin{aligned} \mathbf{R}_{z-y-z} = & \begin{bmatrix} \cos \psi & \sin \psi & 0 \\ -\sin \psi & \cos \psi & 0 \\ 0 & 0 & 1 \end{bmatrix} \begin{bmatrix} \cos \theta & 0 & -\sin \theta \\ 0 & 1 & 0 \\ \sin \theta & 0 & \cos \theta \end{bmatrix} \begin{bmatrix} \cos \phi & \sin \phi & 0 \\ -\sin \phi & \cos \phi & 0 \\ 0 & 0 & 1 \end{bmatrix} \\ = & \begin{bmatrix} \cos \phi \cos \theta \cos \psi - \sin \phi \sin \psi & \cos \theta \cos \psi \sin \phi + \cos \phi \sin \psi & -\cos \psi \sin \theta \\ -\cos \psi \sin \phi - \cos \phi \cos \theta \sin \psi & \cos \phi \cos \psi - \cos \theta \sin \phi \sin \psi & \sin \theta \sin \psi \\ \cos \phi \sin \theta & \sin \phi \sin \theta & \cos \theta \end{bmatrix} \end{aligned} \quad (8)$$

Calculating the nonlinear susceptibility using eq 6 for a bulk material in which molecules adopt random orientations, the azimuthal angle ϕ , tilt angle θ , and twist angle ψ need to be averaged by taking the angle integration (0 to 2π for ϕ and ψ ; 0 to π for θ).

The third-order nonlinear susceptibility tensor $\chi^{(3)}$ has 81 elements. However, many elements may equal to zero due to the symmetry properties of the functional group under consideration. Furthermore, as shown in eqs 4 and 5, CARS signals detected under certain polarization combinations only probe certain elements. For example, the ssss polarization combination only probes $\chi_{yyyy}^{(3)}$. The macroscopic symmetry of the sample can also reduce the number of nonzero terms in $\chi^{(3)}$. For example, for an isotropic bulk material, all the $\chi^{(3)}$ elements with even numbers of x, y, or z indices are zero. In such a case, there are only 21 nonzero tensor elements

In this equation, N is the number density of the molecules that contribute to the CARS signal. R represents the elements of the transformation matrix from the molecular frame (a, b, c) to the lab frame (x, y, z) coordinate system. Such a transformation matrix R is usually a function of three rotational angles: azimuthal angle ϕ , tilt angle θ , and twist angle ψ , as defined in Figure 2 based on the Euler angle definition. The angle brackets here indicate ensemble average. This equation means that the macroscopic third-order nonlinear susceptibility is the ensemble average of the hyperpolarizability of each molecule projected to the lab frame multiplied by the number density of molecules. The transformation matrices of counter-clockwise rotations with respect to x, y, z or a, b, c axes (pointing toward the observer) for α degree are

$$\begin{aligned} \mathbf{R}_{x(\text{or } a)} = & \begin{bmatrix} 1 & 0 & 0 \\ 0 & \cos \alpha & \sin \alpha \\ 0 & -\sin \alpha & \cos \alpha \end{bmatrix} \\ \mathbf{R}_{y(\text{or } b)} = & \begin{bmatrix} \cos \alpha & 0 & -\sin \alpha \\ 0 & 1 & 0 \\ \sin \alpha & 0 & \cos \alpha \end{bmatrix} \\ \mathbf{R}_{z(\text{or } c)} = & \begin{bmatrix} \cos \alpha & \sin \alpha & 0 \\ -\sin \alpha & \cos \alpha & 0 \\ 0 & 0 & 1 \end{bmatrix} \end{aligned} \quad (7)$$

For the three-dimensional rotations in an Euler angle system, there are multiple basic rotation combinations to overlap the two coordinate systems. Each combination consists of three rotation operations. Here, we choose the “z–y–z” rotation combination: the first rotation is with respect to z axis (azimuthal angle ϕ), the second rotation is with respect to y axis (tilt angle θ), the third rotation is with respect to z axis again (twist angle ψ). The resulting transformation matrix is

$$\begin{aligned} \chi_{xxxx}^{(3)} = \chi_{yyyy}^{(3)} = \chi_{zzzz}^{(3)} \\ \chi_{yyzz}^{(3)} = \chi_{zzyy}^{(3)} = \chi_{zzxx}^{(3)} = \chi_{xxzz}^{(3)} = \chi_{xxyy}^{(3)} = \chi_{yyxx}^{(3)} \\ \chi_{yzyz}^{(3)} = \chi_{zyyz}^{(3)} = \chi_{zxzx}^{(3)} = \chi_{xxzz}^{(3)} = \chi_{xyxy}^{(3)} = \chi_{yxxy}^{(3)} \\ \chi_{yzzy}^{(3)} = \chi_{zyyz}^{(3)} = \chi_{zxzx}^{(3)} = \chi_{xxzz}^{(3)} = \chi_{xyyx}^{(3)} = \chi_{yxyx}^{(3)} \\ \chi_{xxxx}^{(3)} = \chi_{xxyy}^{(3)} + \chi_{xyxy}^{(3)} + \chi_{xyyx}^{(3)} \end{aligned} \quad (9)$$

A methyl group is usually treated as having a C_{3v} symmetry. Although the validity of such treatment has been discussed, it is generally accepted that the coupling between the C–H vibration in a methyl group and the vibrational modes of other parts of the molecule can be ignored (i.e., the C_{3v} symmetry treatment

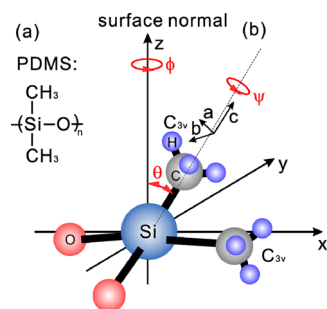


Figure 2. (a) the molecular formula of PDMS. (b) Schematic of a PDMS molecule residue in a lab frame coordinate system (x, y, z) defined in Figure 1a. Each methyl group presents a C_{3v} symmetry. The molecular coordinate of a methyl group is defined as (a, b, c). Azimuthal angle ϕ , tilt angle θ , and twist angle ψ are also defined.

of a methyl group is acceptable).⁶⁰ In this work, we treat a Si-CH₃ group as adopting C_{3v} symmetry for CARS signals analysis. Our results show that such treatment and analysis are acceptable.

The third-order hyperpolarizability $\chi_{ijkl}^{(3)}$ is defined as

$$\gamma_{ijkl}^{(3)} \propto \frac{\partial \alpha_{ij}}{\partial Q_q} \frac{\partial \alpha_{kl}}{\partial Q_q} = \alpha'_{ij} \alpha'_{kl} \quad (10)$$

Here, α'_{ij} and α'_{kl} are Raman polarizability derivatives with respect to the normal mode coordinate of the q^{th} vibrational mode. Therefore, the third-order nonlinear hyperpolarizability that determines CARS functional group vibrational modes can be derived from the Raman tensor derivatives of the same functional group. Next, we will use the bond additivity method to derive the forms of such derivatives for a PDMS methyl group.

2.2. Bond Additivity Method for Methyl Group C-H Stretching Modes. The basic idea of “bond additivity” is to obtain a parameter (e.g., dipole moment, Raman polarizability, etc.) of a molecule by combining the corresponding parameter of each related chemical bond forming the molecule while considering the molecular geometry. For example, using bond additivity method to obtain the polarizability of a certain C-H mode of a methyl group, we can combine the polarizability of each C-H group considering the vibrational modes and methyl group geometry. An individual C-H bond can be considered possessing $C_{\infty v}$ symmetry. Its Raman tensor derivatives satisfy $\alpha'_{aa}/\alpha'_{cc} = \alpha'_{bb}/\alpha'_{cc} = r$, with all other components of the tensor equaling to zero. Here, the single C-H bond coordinate system is defined by (a', b', c') and the c' axis of the molecular coordinate is set along the C-H bond, as depicted in Figure 3a. We can combine the three C-H bonds in a methyl group in the molecular coordinate system (a, b, c) shown in Figure 3b to deduce the Raman tensor derivative of the entire CH₃ group for different vibration modes.

The combining of the three C-H bonds requires the rotation of the single bond coordinate system (Figure 3a) to project each C-H bond to the methyl group coordinate system (Figure 3b). The transformation of the Raman tensor derivative after rotation is

$$\alpha'_{C-H,b} = \mathbf{T} \alpha'_{C-H,a} \mathbf{T}^T \quad (11)$$

\mathbf{T} is the transformation matrix tensor for each bond and \mathbf{T}^T is the transpose of \mathbf{T} . $\alpha'_{C-H,a}$ is the Raman tensor derivative in coordinate 1 (before rotation), whereas $\alpha'_{C-H,b}$ is the Raman tensor derivative in coordinate 2 (after rotation).

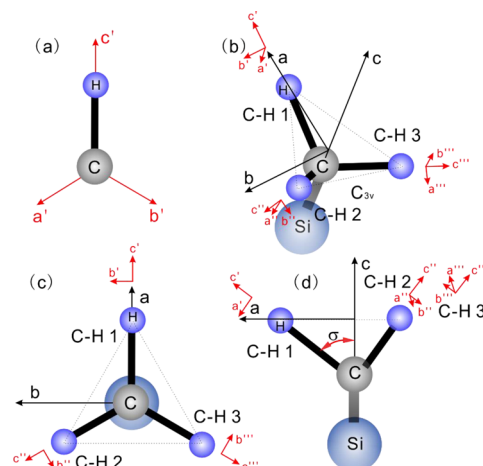


Figure 3. (a) A single C-H bond and the molecular coordinate system (a', b', c') chosen for the bond. (b) A methyl group and its molecular coordinate system (a, b, c). Three C-H bonds and their independent molecular systems are also defined (a', b', c' ; a'', b'', c'' ; a''', b''', c'''). C-H bond 1 is in the a - c plane. The c axis is set along the methyl group principal axis. (c) The “top view” (a - b plane projection) of the picture depicted in (b), the c axis is perpendicular to the paper. (d) The “side view” (a - c plane projection) of the picture depicted in (b), the b axis is perpendicular to the paper.

The Raman tensor derivative of a single C-H bond ($C_{\infty v}$ symmetry) has the form

$$\alpha'_{C-H} = \alpha'_{cc} \begin{bmatrix} r & 0 & 0 \\ 0 & r & 0 \\ 0 & 0 & 1 \end{bmatrix} \quad (12)$$

Each single C-H bond can rotate freely along its principle axis. Therefore, we can choose a coordinate system for the C-H bond 1 (a', b', c') as demonstrated in Figure 3b. Here, the b' axis for the C-H bond is along the b axis defined for the entire methyl group. Figure 3c and d depict such coordinate system from projections on a - b and a - c planes respectively for a clearer visualization. The only rotation required to overlap the (a', b', c') coordinate system with the (a, b, c) system is the rotation of $-\sigma$ angle with respect to b' axis. According to the methyl group geometry, σ is calculated to be $\sim 71^\circ$. We can define this rotation as $\mathbf{R}_{b':-71}$. Thus, we have

$$\alpha'_{C-H1} = \mathbf{R}_{b':-71} \alpha'_{C-H} \mathbf{R}_{b':-71}^T \quad (13)$$

For the second C-H bond, we choose the coordinate (a'', b'', c'') as defined in Figure 3b. Here, b'' axis is perpendicular to the plane formed by C-H bond 2 and the c axis of the methyl group; c'' is along the same C-H bond 2. Two rotations are needed to overlap the (a'', b'', c'') system with the (a, b, c) system: a rotation of -71° with respect to b'' ; after the first rotation, another rotation of -120° with respect to c'' . Thus, we have

$$\alpha'_{C-H2} = \mathbf{R}_{c'':-120} (\mathbf{R}_{b'':-71} \alpha'_{C-H} \mathbf{R}_{b'':-71}^T) \mathbf{R}_{c'':-120}^T \quad (14)$$

Similarly for the third C-H bond we have

$$\alpha'_{C-H3} = \mathbf{R}_{c''':120} (\mathbf{R}_{b''':-71} \alpha'_{C-H} \mathbf{R}_{b''':-71}^T) \mathbf{R}_{c''':120}^T \quad (15)$$

In the process of bond additivity, different vibrational modes need to be taken into consideration. For example, a methyl group with C_{3v} symmetry has three C-H stretching modes. Of these three modes, one is a symmetric stretching (A_1) mode

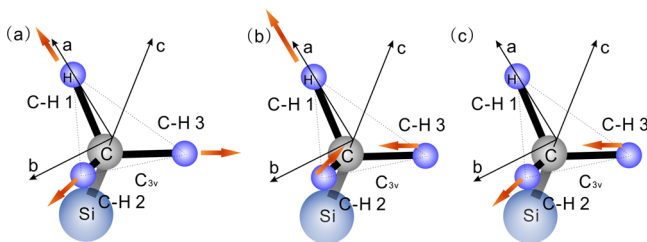


Figure 4. C–H vibrational stretching modes of a methyl group: (a) symmetric A_1 mode; (b) asymmetric E_a mode; (c) asymmetric E_b mode.

while the other two are degenerate asymmetric stretching (E_a and E_b) modes, as demonstrated in Figure 4.

Such vibrational modes can be expressed in the normal mode coordinates^{55,60}

$$Q_{A_1} = \frac{(\Delta r_1 + \Delta r_2 + \Delta r_3)}{(3G_{A_1})^{1/2}}$$

$$Q_{E_a} = \frac{(2\Delta r_1 - \Delta r_2 - \Delta r_3)}{(6G_E)^{1/2}}$$

$$Q_{E_b} = \frac{(\Delta r_2 - \Delta r_3)}{(2G_E)^{1/2}} \quad (16)$$

Here Δr_n is the bond displacement vector along the direction of the n^{th} C–H bond. G_{A_1} and G_E are inverted reduced masses of A_1 and E modes⁶⁰

$$G_{A_1} = \frac{1 + 2\cos \tau}{M_C} + \frac{1}{M_H}$$

$$G_E = \frac{1 - \cos \tau}{M_C} + \frac{1}{M_H} \quad (17)$$

where τ is the H–C–H bond angle which is 109.5° . M_C and M_H are atomic masses of the carbon and hydrogen atoms. We can then obtain $G_{A_1} = 1.03$ and $G_E = 1.11$.

$$\alpha'_{C-H,E} = \alpha'_{C-H,E_a} + \alpha'_{C-H,E_b}$$

$$= \alpha'_{cc} \begin{bmatrix} 0.519 - 0.519r & -0.519 + 0.519r & 0.358 - 0.358r \\ -0.519 + 0.519r & -0.519 + 0.519r & 0.358 - 0.358r \\ 0.358 - 0.358r & 0.358 - 0.358r & 0 \end{bmatrix} \quad (22)$$

Equations 19 and 22 can be used to derive the CARS molecular hyperpolarizability tensor components with eq 10. Furthermore, they can be used to deduce the third-order nonlinear susceptibility of the material for different C–H vibrational modes using eq 6. However, the value “ r ” needs to be known for the quantitative interpretation of the symmetric and asymmetric vibrational spectra. In this work, we performed an empirical approach to determine the value of r using the relationship between r and the Raman depolarization ratio ρ .

2.3. Raman Depolarization Ratio. Raman depolarization can be expressed as^{60,65}

$$\rho = \frac{3\gamma^2}{45\alpha^2 + 4\gamma^2} \quad (23)$$

Here, γ and α are defined by the derivatives of the Raman polarizability tensor elements^{60,65}

We have calculated the Raman tensor derivative for each of the three C–H bonds above. For the A_1 mode as shown in Figure 4a, we can combine the three C–H bonds by simply sum them together and then divided by $(3G_{A_1})^{1/2}$, according to eq 16

$$\alpha'_{C-H,A_1} = (\mathbf{R}_{b';-71}\alpha'_{C-H}\mathbf{R}_{b';-71}^T$$

$$+ \mathbf{R}_{c'';-120}(\mathbf{R}_{b'';-71}\alpha'_{C-H}\mathbf{R}_{b'';-71}^T)\mathbf{R}_{c'';-120}^T$$

$$+ \mathbf{R}_{c'';120}(\mathbf{R}_{b'';-71}\alpha'_{C-H}\mathbf{R}_{b'';-71}^T)\mathbf{R}_{c'';120}^T)/(3G_{A_1})^{1/2} \quad (18)$$

Using eq 7 and 12, we have

$$\alpha'_{C-H,A_1} = \alpha'_{cc}$$

$$\begin{bmatrix} 0.763 + 0.944r & 0 & 0 \\ 0 & 0.763 + 0.944r & 0 \\ 0 & 0 & 0.181 + 1.526r \end{bmatrix} \quad (19)$$

The asymmetric E modes are degenerate for the methyl group, as demonstrated in Figure 4b and c. Using eq 16, we can derive the Raman tensor derivatives of the E modes

$$\alpha'_{C-H,E_a} = (2\mathbf{R}_{b';-71}\alpha'_{C-H}\mathbf{R}_{b';-71}^T$$

$$- \mathbf{R}_{c'';-120}(\mathbf{R}_{b'';-71}\alpha'_{C-H}\mathbf{R}_{b'';-71}^T)\mathbf{R}_{c'';-120}^T$$

$$- \mathbf{R}_{c'';120}(\mathbf{R}_{b'';-71}\alpha'_{C-H}\mathbf{R}_{b'';-71}^T)\mathbf{R}_{c'';120}^T)/(6G_E)^{1/2} \quad (20)$$

$$\alpha'_{C-H,E_b} = (\mathbf{R}_{c'';-120}(\mathbf{R}_{b'';-71}\alpha'_{C-H}\mathbf{R}_{b'';-71}^T)\mathbf{R}_{c'';-120}^T$$

$$- \mathbf{R}_{c'';120}(\mathbf{R}_{b'';-71}\alpha'_{C-H}\mathbf{R}_{b'';-71}^T)\mathbf{R}_{c'';120}^T)/(2G_E)^{1/2} \quad (21)$$

$$\alpha = \frac{1}{3}[\alpha'_{aa} + \alpha'_{bb} + \alpha'_{cc}]$$

$$\gamma^2 = \frac{1}{2}[(\alpha'_{aa} - \alpha'_{bb})^2 + (\alpha'_{bb} - \alpha'_{cc})^2 + (\alpha'_{cc} - \alpha'_{aa})^2$$

$$+ 6(\alpha'_{ab} + \alpha'_{bc} + \alpha'_{ca})^2] \quad (24)$$

For functional groups with C_{3v} symmetry, the Raman tensor derivative elements of the symmetric stretching mode satisfy $\alpha'_{aa}/\alpha'_{cc} = \alpha'_{bb}/\alpha'_{cc} = R$, which can also be seen in eq 19. Other tensor elements equal to zero. This “ R ” is the tensor element ratio of the entire group possessing C_{3v} symmetry (such as a methyl group), which is different from the “ r ” discussed previously, which is the tensor element ratio of a single C–H bond. Here, for a methyl group, from eq 19, we have

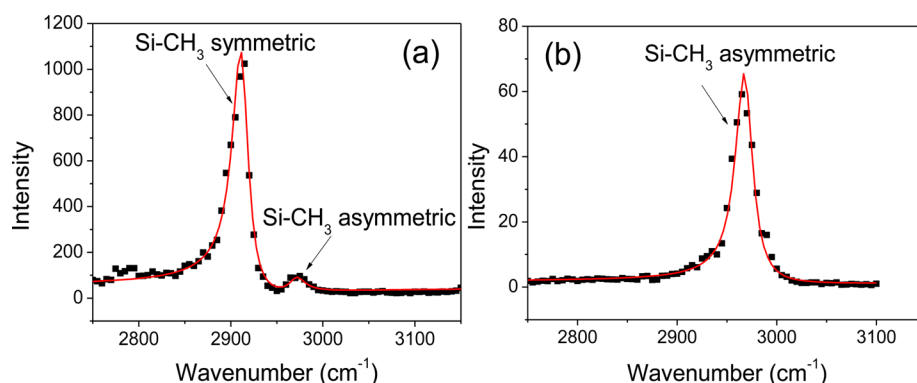


Figure 5. (a) CARS spectrum of the PDMS film collected using ssss polarization combination; (b) CARS spectrum of the PDMS film collected using spps polarization combination. Dots are experimental data, lines are spectral fitting results using eq 2.

$$R = \frac{0.763 + 0.944r}{0.181 + 1.526r} \quad (25)$$

Using $\alpha'_{aa}/\alpha'_{cc} = \alpha'_{bb}/\alpha'_{cc} = R$ and eqs 23–24, we can calculate the depolarization ratio for the methyl symmetric stretching:

$$\rho_s = \frac{3}{4 + 5[(1 + 2R)/(R - 1)]^2} \quad (26)$$

The Raman depolarization ratio ρ_s of methyl C–H symmetric stretching can be measured using Raman experiment. Once ρ_s is known, the values of R and r can be derived. Plugging the r value in eqs 19 and 22, the third-order nonlinear hyperpolarizability $\gamma_{ijkl}^{(3)}$ can be calculated. Further using eqs 10, 6, and 3, quantitative CARS signal peak intensity ratio between symmetric and asymmetric C–H stretching modes of a methyl group can be derived.

3. EXPERIMENTAL RESULTS

In this work, we collected CARS spectra from a PDMS film and analyzed such spectra in order to compare with our theoretical predictions. PDMS is a widely used material in industry and has been extensively studied by Raman spectroscopy. It can generate very strong CARS signals from symmetric and asymmetric methyl C–H stretching. The optical transparency of PDMS can be as low as ~ 250 nm, therefore, using the 532 nm pump/probe laser for the CARS experiment, we did not observe a significant background due to either an enhanced two-photon absorption transition or attenuation due to high sample scattering. A commercial PDMS sample, Sylgard 184 base, was deposited on a fused silica window to form a film of about 50 μm thickness. CARS signal was collected using the reflection geometry as depicted in Figure 1a. The input angles of the pump/probe and Stokes beams used in this experiment were $\sim 62^\circ$ and 58° , respectively.

Details of the CARS system we used in this work have been published previously.¹⁹ Briefly, the system was built based on a commercial SFG vibrational spectrometer. A 532 nm beam was used as the pump/probe beam for CARS experiment. A visible beam tunable from 420 to 680 nm was used as the Stokes beam source. The Stokes beam frequency was tuned continuously while the CARS signal was detected and plotted as a function of Raman transition frequency. In the experiment, blocking the reflection beam from the other side of the silica window is necessary to avoid the overwhelming background generated from the substrate. The CARS spectra were collected in the ssss and spps polarization combinations.

The CARS spectrum of PDMS in C–H range using ssss polarization is shown in Figure 5a. The spectrum has two peaks: the dominant peak centered at 2912 cm^{-1} is due to the symmetric C–H stretching of the Si–CH₃ group, whereas the other weaker peak centered at 2971 cm^{-1} is from the asymmetric C–H stretching of the same group. CARS spectral fitting was performed to obtain quantitative analysis of these two peaks. The spectral fitting was carried out using eq 2 by combining the two-photon resonant contribution with the virtual state nonresonant term into one nonresonant constant $\chi_{NR}^{(3)}$. The fitting results are listed in Table 1. The symmetric

Table 1. Spectral Fitting Parameters Used for the Fitting in Figure 5

(a)	offset (ssss)		35.0 a.u.
	$\chi_{NR}^{(3)}$ (ssss)		−3.9 a.u.
	symmetric mode (ssss)	A_{A_1}	328.7 a.u.
		ω_{A_1}	2912 cm^{-1}
		Γ_{A_1}	10.5 cm^{-1}
(b)	asymmetric mode (ssss)	A_E	66.7 a.u.
		ω_E	2971 cm^{-1}
		Γ_E	10.5 cm^{-1}
	offset (spps)		1.3 a.u.
	$\chi_{NR}^{(3)}$ (spps)		−0.6 a.u.
	asymmetric mode (spps)	A_E	83.4 a.u.
		ω_E	2968 cm^{-1}
		Γ_E	10.5 cm^{-1}

and asymmetric C–H stretching peak strength ratio can be calculated as

$$\frac{\chi_{ssss,s}^{(3)}}{\chi_{ssss,as}^{(3)}} = \frac{(A_{A_1}/\Gamma_{A_1})}{(A_E/\Gamma_E)} \approx 4.93$$

In the spectrum collected using the spps polarization, only one peak centered at around 2968 cm^{-1} was detected, due to the C–H asymmetric stretching of the methyl group. No signal from the symmetric stretching mode at $\sim 2910\text{ cm}^{-1}$ was detected. The spectral fitting of this asymmetric stretching peak was also performed and the results are also listed in Table 1.

CARS spectra of PDMS collected using different polarization combinations show significantly unique lineshapes. Additionally, the symmetric and asymmetric C–H stretching peaks in the ssss spectrum have very different intensities. In the next section, we will deduce the symmetric and asymmetric C–H

stretching peak strength ratio using the bond additivity method developed above and compare the theoretical results with these experimental data.

4. DISCUSSION

In section 2, we stated that in order to theoretically calculate the third-order nonlinear susceptibility tensor element ratio corresponding to the symmetric and asymmetric stretching modes of a methyl group, Raman depolarization ratio of the symmetric stretching mode needs to be known (in order to obtain the value of r). In this work, PDMS was chosen as an example for quantitative methyl group spectral analysis since the Raman depolarization ratio of PDMS has been well characterized. From previous publications, we know that with zero extension ratio (used in this work), $\rho_{s,PDMS}$ ranges from 0.018 to 0.022 for the methyl symmetric stretching.^{66,67} The molecular weight of the PDMS does not significantly alter the depolarization ratio value.^{66,67} Here, we will adopt this value range for our calculation.

Using eq 26 we can determine that R is in the range of 1.8 to 2.0. There are two possible R solutions corresponding to each $\rho_{s,PDMS}$ value. Here, we only choose the one that gives $R > 1$, because for C_{3v} symmetry, generally $1 < R < 4$.⁶⁰ We can then obtain the value of r using eq 25, and its value is in the range of 0.24 to 0.20.

We can plug our derived r value into eqs 19 and 22 to obtain Raman tensor derivatives for methyl symmetric and asymmetric stretching modes. Furthermore, we can insert eqs 19 and 22 into eqs 10 and 6 and average all the azimuthal, tilt, and twist angles to derive the values of the susceptibility elements which can provide resonance strength ratio of symmetric and asymmetric modes.

Equation 6 can be written in another form for bulk materials with random molecular orientations

$$\chi^{(3)} = \frac{N}{4\pi^3} \int_0^\pi \int_0^{2\pi} \int_0^{2\pi} \mathbf{R} \otimes \mathbf{R} \otimes \mathbf{R} \otimes \mathbf{R} \cdot \gamma^{(3)} \sin \theta d\phi d\psi d\theta \quad (27)$$

In this expression, $\chi^{(3)}$ is a nonlinear susceptibility matrix of dimension 81 by 1. $\gamma^{(3)}$ is the third-order molecular hyperpolarizability matrix with identical dimension. \mathbf{R} is the rotation transformation matrix which is defined in eq 8. The angular average was performed by integrating from 0 to 2π for ϕ and ψ , and from 0 to π for θ , then multiplying by $1/4\pi^3$. The sign \otimes means Kronecker product.

Another way to express $\gamma^{(3)}$ is to use a 9 by 9 matrix formed by $\alpha' \otimes \alpha'$, where each α' is a 3 by 3 matrix. The detailed $\gamma^{(3)}$ matrix form (detailed element arrangements) is shown in the Supporting Information. If we use such expression (9 by 9 matrix), $\chi^{(3)}$ satisfies

$$\chi^{(3)} = \frac{Nc}{4\pi^3} \int_0^\pi \int_0^{2\pi} \int_0^{2\pi} \mathbf{R} \otimes \mathbf{R} (\alpha' \otimes \alpha') (\mathbf{R} \otimes \mathbf{R})^T \sin \theta d\phi d\psi d\theta \quad (28)$$

Here, $\chi^{(3)}$ is a 9 by 9 matrix representing the same susceptibility elements as in eq 27. c is a constant ratio between $\gamma_{ijkl}^{(3)}$ and $\alpha'_{ij}\alpha'_{kl}$ as shown in eq 10. Mathematically, eqs 27 and 28 are identical expressions; only the matrix elements have been rearranged.

When we take the susceptibility ratio between the symmetric and asymmetric stretching modes in a certain polarization combination

$$\frac{\chi_{ss}^{(3)}}{\chi_{as}^{(3)}} = \frac{\int_0^\pi \int_0^{2\pi} \int_0^{2\pi} \mathbf{R} \otimes \mathbf{R} (\alpha'_{C-H,A1} \otimes \alpha'_{C-H,A1}) (\mathbf{R} \otimes \mathbf{R})^T \sin \theta d\phi d\psi d\theta}{\int_0^\pi \int_0^{2\pi} \int_0^{2\pi} \mathbf{R} \otimes \mathbf{R} (\alpha'_{C-H,E} \otimes \alpha'_{C-H,E}) (\mathbf{R} \otimes \mathbf{R})^T \sin \theta d\phi d\psi d\theta} \quad (29)$$

Inserting eqs 8, 19, and 22 into eq 29 with the derived value of r (here, we used minimum and maximum values 0.20 and 0.24), we can obtain all the third-order nonlinear susceptibility elements relations for symmetric and asymmetric modes. The detailed results are shown in the Supporting Information. We are interested in the ratio $\chi_{yyyy,s}^{(3)}/\chi_{yyyy,as}^{(3)}$ which is measured using CARS experiment in the ssss polarization (the CARS signal measured using the ssss polarization combination is only related to $\chi_{yyyy}^{(3)}$ as shown in eq 4). We used Mathematica 7.0 to calculate such results and obtained: $\chi_{yyyy,s}^{(3)}/\chi_{yyyy,as}^{(3)} = 4.7$ when $r = 0.20$; $\chi_{yyyy,s}^{(3)}/\chi_{yyyy,as}^{(3)} = 5.9$ when $r = 0.24$.

In the previous CARS experiment, signals generated by the symmetric and asymmetric modes of a methyl group were detected in the same ssss polarization combination. Therefore, the Fresnel coefficients in eq 4 are the same for both modes. For the measured peak intensity ratio, we have $\chi_{yyyy,s}^{(3)}/\chi_{yyyy,as}^{(3)} = \chi_{ssss,s}^{(3)}/\chi_{ssss,as}^{(3)} = 4.93$ (from Table 1). This measured value falls into the range from 4.7 to 5.9 as we calculated above, indicating that our theoretical work can be used to quantitatively interpret and predict the CARS vibrational stretching intensities of different methyl vibrational modes.

Using the bond additivity method, we can also calculate some characteristics of the vibrational signals detected using other polarization combinations. For example, from eq 5 we know that $\chi_{eff,spps}^{(3)}$ is related to $\chi_{yxxxy}^{(3)}$, $\chi_{yxxzy}^{(3)}$, and $\chi_{yzzy}^{(3)}$. Assuming that the PDMS film is isotropic and a methyl group is adopting C_{3v} symmetry, susceptibilities tensor elements $\chi_{yxxzy}^{(3)}$ and $\chi_{yzzy}^{(3)}$ equal to zero, as we showed in eq 9. Therefore, $\chi_{eff,spps}^{(3)}$ is only related to $\chi_{yxxxy}^{(3)}$ and $\chi_{yzzzy}^{(3)}$. From eq 9, we have $\chi_{yxxxy}^{(3)} = \chi_{yzzzy}^{(3)}$. On the basis of our calculation results (shown in the Supporting Information), for the $r = 0.20$ case

$$\frac{\chi_{yyyy,s}^{(3)}}{\chi_{yxxxy,s}^{(3)}} = \frac{\chi_{yyyy,s}^{(3)}}{\chi_{yzzzy,s}^{(3)}} = \frac{0.42}{0.0088} \approx 48$$

$$\frac{\chi_{yyyy,as}^{(3)}}{\chi_{yxxxy,as}^{(3)}} = \frac{\chi_{yyyy,as}^{(3)}}{\chi_{yzzzy,as}^{(3)}} = \frac{0.088}{0.066} \approx 1.3$$

If we want to compare the CARS signal strengths collected using different polarization combinations, Fresnel coefficients need to be considered, as shown in eq 5. It is difficult to deduce the exact Fresnel factors for the experiments. However, the approximate (the order of magnitude) values can be obtained. As detailed in the Supporting Information, we derived

$$\frac{\chi_{ssss}^{(3)}}{\chi_{spps}^{(3)}} \approx 0.79 \frac{\chi_{yyyy}^{(3)}}{\chi_{yxxxy}^{(3)}} \quad (30)$$

Inserting the susceptibility tensor element ratios we obtained for the methyl symmetric and asymmetric stretching modes into eq 30, we have

$$\frac{\chi_{ssss,s}^{(3)}}{\chi_{spps,s}^{(3)}} \approx 0.79 \frac{\chi_{yyyy,s}^{(3)}}{\chi_{yxyx,s}^{(3)}} \approx 38$$

$$\frac{\chi_{ssss,as}^{(3)}}{\chi_{spps,as}^{(3)}} \approx 0.79 \frac{\chi_{yyyy,as}^{(3)}}{\chi_{yxyx,as}^{(3)}} \approx 1$$

These results indicate that for the symmetric stretching mode, the value of third-order susceptibility element detected using the spps polarization combination is much smaller than that detected using the ssss polarization. For the asymmetric stretching mode, however, the values are similar. Because the CARS signal intensity is proportional to the square of the nonlinear susceptibility as shown in eq 1, in the spps polarization, the symmetric stretching signal intensity should be approximately 1400 times weaker than that in the ssss polarization; however, CARS signal intensities for the asymmetric stretching in two polarizations are similar. The ssss signal intensities for the methyl C–H symmetric and asymmetric stretching modes (as shown in Figure 5a) are ~ 1000 a.u. and ~ 50 a.u., respectively. Therefore, we can predict that in the spps polarization spectrum, the dominating peak should be the methyl asymmetric stretching mode, with no resolvable signal from the symmetric stretching mode ($1000/1400 \approx 0.7$ a.u., below the noise level). The CARS spectrum of the PDMS film collected using spps polarization is shown in Figure 5b. We found that, as predicted, only strong asymmetric stretching peak center at ~ 2968 cm^{-1} could be detected. No symmetric stretching signal at ~ 2910 cm^{-1} was resolvable. The fitting results show that $A_{spps,E}/\Gamma_{spps,E} \approx 7.98$, which is slightly different from $A_{ssss,E}/\Gamma_{ssss,E} \approx 6.38$ measured in the ssss polarization. This gives $\chi_{ssss,as}^{(3)}/\chi_{spps,as}^{(3)} \approx 1.25$, which is slightly bigger than 1 (obtained from our calculation). Such small difference perhaps caused by the inaccuracy in the Fresnel coefficient calculation for different polarization combinations (input angle error, refractive index error, laser fluctuations in different polarizations, etc.). The susceptibility matrices calculated for the methyl symmetric and asymmetric modes using $r = 0.20$ and $r = 0.24$ are shown in the Supporting Information. The above spectral analysis in spps polarization is based on $r = 0.20$; The value $r = 0.24$ gives similar conclusions.

In this work, the CARS experiment was performed using a reflection BOXCAR geometry.⁶⁸ However, the results obtained here are also valid for the collinear CARS configuration used for CARS imaging. In a laser scanning CARS microscopy system, two input laser beams are usually collimated collinearly, directed perpendicularly to the sample and focused using objective lenses. In such a geometry, the ssss polarization is defined as the two input laser beams (pump/probe and Stokes) entering the sample with the same linear polarization; the spps polarization requires the two linearly polarized input laser beams enter the sample with perpendicular polarizations. For the first case, if CARS is used to image PDMS methyl groups, the symmetric vibrational stretching signal should dominate the spectrum; for the latter case, the asymmetric stretching signal should dominate the spectrum, with an overall spectral intensity significant lower as compared to the intensity of the symmetric mode measured using an ssss configuration.

Although more complicated molecules may have spectral feature overlapping or energy coupling between different vibrational modes, we show that bond additivity method can be used to help explain methyl group vibrational properties in ideal sample conditions using PDMS (with isolated Raman bands). This theoretical approach is an important start for such quantitative CARS spectral analysis based on molecular geometries. Modifications of bond additivity method might be needed for the analysis of more complicated molecules that will be performed in the future.

5. CONCLUSION

A theoretical method for the quantitative interpretation of methyl group CARS spectra was developed in this research. Methyl symmetric and asymmetric C–H vibrational stretching intensity ratios measured in different polarization combinations were calculated using the bond additivity model and the Raman depolarization ratio. Additionally, a home-built BOXCAR system was used to measure CARS signal from a PDMS film in the C–H range. The results from theoretical calculations agreed well with experimental data taken on the PDMS film. We introduced a way to quantitatively interpret and predict the CARS vibrational spectral intensity ratios of different vibrational modes in different polarization combinations based on bond additivity method and Raman depolarization ratio. This work help develop in-depth understanding in vibrational stretching properties measured by CARS spectroscopy. Quantitative understanding and interpretation of CARS spectrum can add knowledge in basic third-order nonlinear spectroscopy theory and will have important applications in CARS spectroscopy and microscopy for advanced signal analysis.

■ ASSOCIATED CONTENT

Supporting Information

Fresnel coefficient calculation, the general form of third-order nonlinear hyperpolarizability matrix, the susceptibility matrices calculated using $r = 0.20$ and $r = 0.24$. This material is available free of charge via the Internet at <http://pubs.acs.org>.

■ AUTHOR INFORMATION

Corresponding Author

*E-mail: zhangchi@umich.edu. Tel.: (734) 389-5895.

Present Address

§AbbVie, 1 North Waukegan Road, North Chicago, Illinois 60064, United States

Notes

The authors declare no competing financial interest.

■ ACKNOWLEDGMENTS

We sincerely thank Dr. Zhan Chen for his contribution in the discussion and suggestion of the work, the editing of the paper, as well as the financial and equipment support for this research.

■ REFERENCES

- (1) Maker, P.; Terhune, R. Study of Optical Effects Due to an Induced Polarization Third Order in the Electric Field Strength. *Phys. Rev.* **1965**, *137*, A801.
- (2) Tolles, W. M.; Nibler, J.; McDonald, J.; Harvey, A. A Review of the Theory and Application of Coherent Anti-Stokes Raman Spectroscopy (CARS). *Appl. Spectrosc.* **1977**, *31*, 253–271.
- (3) Régner, P. R.; Moya, F.; Taran, J. P. E. Gas Concentration Measurement by Coherent Raman Anti-Stokes Scattering. *AIAA J.* **1974**, *12*, 826–831.

- (4) Schrötter, H.; Berger, H.; Boquillon, J.; Lavorel, B.; Millot, G. High-Resolution Non-Linear Raman Spectroscopy in Gases. *J. Raman Spectrosc.* **1990**, *21*, 781–789.
- (5) Moya, F.; Druet, S. A. J.; Taran, J. P. E. Gas Spectroscopy and Temperature Measurement by Coherent Raman Anti-Stokes Scattering. *Opt. Commun.* **1975**, *13*, 169–174.
- (6) Hall, R. CARS Spectra of Combustion Gases. *Combust. Flame* **1979**, *35*, 47–60.
- (7) Klick, D.; Marko, K. A.; Rimai, L. Broadband Single-Pulse CARS Spectra in a Fired Internal Combustion Engine. *Appl. Opt.* **1981**, *20*, 1178–1181.
- (8) Eckbreth, A. C. *Laser Diagnostics for Combustion Temperature and Species*; CRC Press: Boca Raton, FL, 1996; Vol. 3.
- (9) Hassel, E. P.; Linow, S. Laser Diagnostics for Studies of Turbulent Combustion. *Meas. Sci. Technol.* **2000**, *11*, R37.
- (10) Miles, R.; Laufer, G.; Bjorklund, G. Coherent Anti-Stokes Raman Scattering in a Hollow Dielectric Waveguide. *Appl. Phys. Lett.* **1977**, *30*, 417–419.
- (11) Itzkan, I.; Leonard, D. A. Observation of Coherent Anti-Stokes Raman Scattering from Liquid Water. *Appl. Phys. Lett.* **1975**, *26*, 106–108.
- (12) Joo, T.; Albrecht, A. Femtosecond Time-Resolved Coherent Anti-Stokes Raman Spectroscopy of Liquid Benzene: A Kubo Relaxation Function Analysis. *J. Chem. Phys.* **1993**, *99*, 3244–3251.
- (13) Nestor, J.; Spiro, T. G.; Klauminzer, G. Coherent Anti-Stokes Raman Scattering (CARS) Spectra, with Resonance Enhancement, of Cytochrome C and Vitamin B12 in Dilute Aqueous Solution. *Proc. Natl. Acad. Sci. U. S. A.* **1976**, *73*, 3329–3332.
- (14) Schmidt, S. C.; Moore, D. S. Vibrational Spectroscopy of High-Temperature, Dense Molecular Fluids by Coherent Anti-Stokes Raman Scattering. *Acc. Chem. Res.* **1992**, *25*, 427–432.
- (15) Moore, D.; Schmidt, S.; Shaw, M.; Johnson, J. Coherent Anti-Stokes Raman Spectroscopy of Shock-Compressed Liquid Nitrogen. *J. Chem. Phys.* **1989**, *90*, 1368–1376.
- (16) Hellwig, H.; Daniels, W. B.; Hemley, R. J.; Mao, H. K.; Gregoryanz, E.; Yu, Z. Coherent Anti-Stokes Raman Scattering Spectroscopy of Solid Nitrogen to 22 GPa. *J. Chem. Phys.* **2001**, *115*, 10876–10882.
- (17) Wen, X.; Chen, S.; Dlott, D. D. Time-Resolved Three-Color Coherent Raman Scattering Applied to Polycrystalline and Opaque Solids. *J. Opt. Soc. Am. B* **1991**, *8*, 813–819.
- (18) Grisch, F.; Pealat, M.; Bouchardy, P.; Taran, J.; Bar, I.; Heflinger, D.; Rosenwaks, S. Real Time Diagnostics of Detonation Products from Lead Azide Using Coherent Anti-Stokes Raman Scattering. *Appl. Phys. Lett.* **1991**, *59*, 3516–3518.
- (19) Zhang, C.; Wang, J.; Khmaladze, A.; Liu, Y.; Ding, B.; Jasensky, J.; Chen, Z. Examining Surface and Bulk Structures Using Combined Nonlinear Vibrational Spectroscopies. *Opt. Lett.* **2011**, *36*, 2272–2274.
- (20) Portnov, A.; Rosenwaks, S.; Bar, I. Detection of Particles of Explosives via Backward Coherent Anti-Stokes Raman Spectroscopy. *Appl. Phys. Lett.* **2008**, *93*, 041115.
- (21) Katz, O.; Natan, A.; Silberberg, Y.; Rosenwaks, S. Standoff Detection of Trace Amounts of Solids by Nonlinear Raman Spectroscopy Using Shaped Femtosecond Pulses. *Appl. Phys. Lett.* **2008**, *92*, 171116.
- (22) Li, H.; Harris, D. A.; Xu, B.; Wrzesinski, P. J.; Lozovoy, V. V.; Dantus, M. Coherent Mode-Selective Raman Excitation Towards Standoff Detection. *Opt. Express* **2008**, *16*, 5499–5504.
- (23) Natan, A.; Levitt, J. M.; Graham, L.; Katz, O.; Silberberg, Y. Standoff Detection via Single-Beam Spectral Notch Filtered Pulses. *Appl. Phys. Lett.* **2012**, *100*, 051111.
- (24) Portnov, A.; Bar, I.; Rosenwaks, S. Highly Sensitive Standoff Detection of Explosives via Backward Coherent Anti-Stokes Raman Scattering. *Appl. Phys. B: Laser Opt.* **2010**, *98*, 529–535.
- (25) Bremer, M. T.; Wrzesinski, P. J.; Butcher, N.; Lozovoy, V. V.; Dantus, M. Highly Selective Standoff Detection and Imaging of Trace Chemicals in a Complex Background Using Single-Beam Coherent Anti-Stokes Raman Scattering. *Appl. Phys. Lett.* **2011**, *99*, 101109.
- (26) Cheng, J. X.; Xie, X. S. Coherent Anti-Stokes Raman Scattering Microscopy: Instrumentation, Theory, and Applications. *J. Phys. Chem. B* **2004**, *108*, 827–840.
- (27) Rodriguez, L. G.; Lockett, S. J.; Holtom, G. R. Coherent Anti-Stokes Raman Scattering Microscopy: A Biological Review. *Cytometry A* **2006**, *69*, 779–791.
- (28) El-Diasty, F. Coherent Anti-Stokes Raman Scattering: Spectroscopy and Microscopy. *Vib. Spectrosc.* **2011**, *55*, 1–37.
- (29) Duncan, M. D.; Reintjes, J.; Manuccia, T. Scanning Coherent Anti-Stokes Raman Microscope. *Opt. Lett.* **1982**, *7*, 350–352.
- (30) Evans, C. L.; Xie, X. S. Coherent Anti-Stokes Raman Scattering Microscopy: Chemical Imaging for Biology and Medicine. *Annu. Rev. Anal. Chem.* **2008**, *1*, 883–909.
- (31) Zumbusch, A.; Holtom, G. R.; Xie, X. S. Three-Dimensional Vibrational Imaging by Coherent Anti-Stokes Raman Scattering. *Phys. Rev. Lett.* **1999**, *82*, 4142–4145.
- (32) Evans, C. L.; Potma, E. O.; Puoris'haag, M.; Côté, D.; Lin, C. P.; Xie, X. S. Chemical Imaging of Tissue in Vivo with Video-Rate Coherent Anti-Stokes Raman Scattering Microscopy. *Proc. Natl. Acad. Sci. U. S. A.* **2005**, *102*, 16807–16812.
- (33) Cheng, J. X.; Jia, Y. K.; Zheng, G.; Xie, X. S. Laser-Scanning Coherent Anti-Stokes Raman Scattering Microscopy and Applications to Cell Biology. *Biophys. J.* **2002**, *83*, 502–509.
- (34) Cheng, J. X.; Book, L. D.; Xie, X. S. Polarization Coherent Anti-Stokes Raman Scattering Microscopy. *Opt. Lett.* **2001**, *26*, 1341–1343.
- (35) Cheng, J. X.; Volkmer, A.; Xie, X. S. Theoretical and Experimental Characterization of Coherent Anti-Stokes Raman Scattering Microscopy. *J. Opt. Soc. Am. B* **2002**, *19*, 1363–1375.
- (36) Volkmer, A.; Cheng, J. X.; Xie, X. S. Vibrational Imaging with High Sensitivity via Epitdetected Coherent Anti-Stokes Raman Scattering Microscopy. *Phys. Rev. Lett.* **2001**, *87*, 023901.
- (37) Potma, E. O.; Evans, C. L.; Xie, X. S. Heterodyne Coherent Anti-Stokes Raman Scattering (CARS) Imaging. *Opt. Lett.* **2006**, *31*, 241–243.
- (38) Yue, S.; Slipchenko, M. N.; Cheng, J. X. Multimodal Nonlinear Optical Microscopy. *Laser Photonics Rev.* **2011**, *5*, 496–512.
- (39) Potma, E. O.; Xie, X. S. Detection of Single Lipid Bilayers with Coherent Anti-Stokes Raman Scattering (CARS) Microscopy. *J. Raman Spectrosc.* **2003**, *34*, 642–650.
- (40) Cheng, J. X.; Volkmer, A.; Book, L. D.; Xie, X. S. Multiplex Coherent Anti-Stokes Raman Scattering Microspectroscopy and Study of Lipid Vesicles. *J. Phys. Chem. B* **2002**, *106*, 8493–8498.
- (41) Nan, X.; Cheng, J. X.; Xie, X. S. Vibrational Imaging of Lipid Droplets in Live Fibroblast Cells with Coherent Anti-Stokes Raman Scattering Microscopy. *J. Lipid Res.* **2003**, *44*, 2202–2208.
- (42) Zumbusch, A.; Langbein, W.; Borri, P. Nonlinear Vibrational Microscopy Applied to Lipid Biology. *Prog. Lipid Res.* **2013**, *52*, 615–632.
- (43) Lin, C. Y.; Suhaimi, J. L.; Nien, C. L.; Miljković, M. D.; Diem, M.; Jester, J. V.; Potma, E. O. Picosecond Spectral Coherent Anti-Stokes Raman Scattering Imaging with Principal Component Analysis of Meibomian Glands. *J. Biomed. Opt.* **2011**, *16*, 021104–021104–021109.
- (44) Cheng, J. X.; Volkmer, A.; Book, L. D.; Xie, X. S. An Epitdetected Coherent Anti-Stokes Raman Scattering (E-CARS) Microscope with High Spectral Resolution and High Sensitivity. *J. Phys. Chem. B* **2001**, *105*, 1277–1280.
- (45) Marks, D. L.; Vinegoni, C.; Bredfeldt, J. S.; Boppart, S. A. Interferometric Differentiation between Resonant Coherent Anti-Stokes Raman Scattering and Nonresonant Four-Wave-Mixing Processes. *Appl. Phys. Lett.* **2004**, *85*, 5787–5789.
- (46) Dudovich, N.; Oron, D.; Silberberg, Y. Single-Pulse Coherently Controlled Nonlinear Raman Spectroscopy and Microscopy. *Nature* **2002**, *418*, 512–514.
- (47) Shi, K.; Li, H.; Xu, Q.; Psaltis, D.; Liu, Z. Coherent Anti-Stokes Raman Holography for Chemically Selective Single-Shot Nonscanning 3D Imaging. *Phys. Rev. Lett.* **2010**, *104*, 093902.

- (48) Kee, T. W.; Cicerone, M. T. Simple Approach to One-Laser, Broadband Coherent Anti-Stokes Raman Scattering Microscopy. *Opt. Lett.* **2004**, *29*, 2701–2703.
- (49) Bégin, S.; Burgoyne, B.; Mercier, V.; Villeneuve, A.; Vallée, R.; Côté, D. Coherent Anti-Stokes Raman Scattering Hyperspectral Tissue Imaging with a Wavelength-Swept System. *Biomed. Opt. Express* **2011**, *2*, 1296–1306.
- (50) Day, J. P.; Domke, K. F.; Rago, G.; Kano, H.; Hamaguchi, H. O.; Vartiainen, E. M.; Bonn, M. Quantitative Coherent Anti-Stokes Raman Scattering (CARS) Microscopy. *J. Phys. Chem. B* **2011**, *115*, 7713–7725.
- (51) Liu, Y.; Lee, Y. J.; Cicerone, M. T. Broadband CARS Spectral Phase Retrieval Using a Time-Domain Kramers–Kronig Transform. *Opt. Lett.* **2009**, *34*, 1363–1365.
- (52) Cicerone, M. T.; Aamer, K. A.; Lee, Y. J.; Vartiainen, E. Maximum Entropy and Time-Domain Kramers–Kronig Phase Retrieval Approaches are Functionally Equivalent for CARS Microspectroscopy. *J. Raman Spectrosc.* **2012**, *43*, 637–643.
- (53) Davis, R. P.; Moad, A. J.; Goeken, G. S.; Wampler, R. D.; Simpson, G. J. Selection Rules and Symmetry Relations for Four-Wave Mixing Measurements of Uniaxial Assemblies. *J. Phys. Chem. B* **2008**, *112*, 5834–5848.
- (54) Hirose, C.; Akamatsu, N.; Domen, K. Formulas for the Analysis of the Surface SFG Spectrum and Transformation Coefficients of Cartesian SFG Tensor Components. *Appl. Spectrosc.* **1992**, *46*, 1051–1072.
- (55) Hirose, C.; Akamatsu, N.; Domen, K. Formulas for the Analysis of Surface Sum-Frequency Generation Spectrum by CH Stretching Modes of Methyl and Methylene Groups. *J. Chem. Phys.* **1992**, *96*, 997–1004.
- (56) Wang, H. F.; Gan, W.; Lu, R.; Rao, Y.; Wu, B. H. Quantitative Spectral and Orientational Analysis in Surface Sum Frequency Generation Vibrational Spectroscopy (SFG-VS). *Int. Rev. Phys. Chem.* **2005**, *24*, 191–256.
- (57) Wei, X.; Zhuang, X.; Hong, S. C.; Goto, T.; Shen, Y. Sum-Frequency Vibrational Spectroscopic Study of a Rubbed Polymer Surface. *Phys. Rev. Lett.* **1999**, *82*, 4256–4259.
- (58) Zhuang, X.; Miranda, P.; Kim, D.; Shen, Y. Mapping Molecular Orientation and Conformation at Interfaces by Surface Nonlinear Optics. *Phys. Rev. B* **1999**, *59*, 12632–12640.
- (59) Zhang, C.; Chen, Z. Probing Molecular Structures of Poly(Dimethylsiloxane) at Buried Interfaces in Situ. *J. Phys. Chem. C* **2013**, *117*, 3903–3914.
- (60) Wu, H.; Zhang, W. K.; Gan, W.; Cui, Z. F.; Wang, H. F. An Empirical Approach to the Bond Additivity Model in Quantitative Interpretation of Sum Frequency Generation Vibrational Spectra. *J. Chem. Phys.* **2006**, *125*, 133203.
- (61) Wei, X.; Hong, S. C.; Zhuang, X.; Goto, T.; Shen, Y. Nonlinear Optical Studies of Liquid Crystal Alignment on a Rubbed Polyvinyl Alcohol Surface. *Phys. Rev. E: Stat., Nonlinear, Soft Matter Phys.* **2000**, *62*, 5160–5172.
- (62) Nguyen, K. T.; Le Clair, S. V.; Ye, S.; Chen, Z. Orientation Determination of Protein Helical Secondary Structures Using Linear and Nonlinear Vibrational Spectroscopy. *J. Phys. Chem. B* **2009**, *113*, 12169–12180.
- (63) Nguyen, K. T.; King, J. T.; Chen, Z. Orientation Determination of Interfacial β -Sheet Structures in Situ. *J. Phys. Chem. B* **2010**, *114*, 8291–8300.
- (64) Zhang, C.; Myers, J. N.; Chen, Z. Elucidation of Molecular Structures at Buried Polymer Interfaces and Biological Interfaces Using Sum Frequency Generation Vibrational Spectroscopy. *Soft Matter* **2013**, *9*, 4738–4761.
- (65) Allemand, C. D. Depolarization Ratio Measurements in Raman Spectrometry. *Appl. Spectrosc.* **1970**, *24*, 348–353.
- (66) Maxfield, J.; Shepherd, I. Investigation of Molecular Isomerism in Polydimethylsiloxane by Raman Scattering. *Chem. Phys.* **1973**, *2*, 433–444.
- (67) Maxfield, J.; Shepherd, I. Temperature and Strain Dependence of the Raman Depolarization in Poly(dimethylsiloxane). *Chem. Phys. Lett.* **1973**, *19*, 541–545.
- (68) Bloembergen, N.; Chen, K. H.; Lü, C. Z.; Mazur, E. Multiplex Pure Rotational Coherent Anti-Stokes Raman Spectroscopy in a Molecular Beam. *J. Raman Spectrosc.* **1990**, *21*, 819–825.